



HAL
open science

Copper Hyper-Stoichiometry: The Key for the Optimization of Thermoelectric Properties in Stannoidite $\text{Cu}_{8+x}\text{Fe}_{3-x}\text{Sn}_2\text{S}_{12}$

Ventrapati Pavan Kumar, Tristan Barbier, Vincent Caignaert, Bernard Raveau, Ramzy Daou, Bernard Malaman, Gérard Le Caër, P. Lemoine, Emmanuel Guilmeau

► **To cite this version:**

Ventrapati Pavan Kumar, Tristan Barbier, Vincent Caignaert, Bernard Raveau, Ramzy Daou, et al.. Copper Hyper-Stoichiometry: The Key for the Optimization of Thermoelectric Properties in Stannoidite $\text{Cu}_{8+x}\text{Fe}_{3-x}\text{Sn}_2\text{S}_{12}$. *Journal of Physical Chemistry C*, 2017, 121 (30), pp.16454-16461. 10.1021/acs.jpcc.7b02068 . hal-01580457

HAL Id: hal-01580457

<https://univ-rennes.hal.science/hal-01580457>

Submitted on 14 Sep 2017

HAL is a multi-disciplinary open access archive for the deposit and dissemination of scientific research documents, whether they are published or not. The documents may come from teaching and research institutions in France or abroad, or from public or private research centers.

L'archive ouverte pluridisciplinaire **HAL**, est destinée au dépôt et à la diffusion de documents scientifiques de niveau recherche, publiés ou non, émanant des établissements d'enseignement et de recherche français ou étrangers, des laboratoires publics ou privés.

1
2
3
4
5
6
7
8
9
10
11
12
13
14
15
16
17
18
19
20
21
22
23
24
25
26
27
28
29
30
31
32
33
34
35
36
37
38
39
40
41
42
43
44
45
46
47
48
49
50
51
52
53
54
55
56
57
58
59
60

Copper Hyper-stoichiometry, the Key for the Optimization of Thermoelectric Properties in Stannoidite $\text{Cu}_{8+x}\text{Fe}_{3-x}\text{Sn}_2\text{S}_{12}$

*Ventrapati Pavan Kumar,[†] Tristan Barbier,[†] Vincent Caignaert,[†] Bernard Raveau,[†] Ramzy
Daou,[†] Bernard Malaman,[‡] Gérard Le Caër,[#] Pierric Lemoine,[§] and Emmanuel Guilmeau^{*†}*

[†] Laboratoire CRISMAT, UMR 6508 CNRS/ENSICAEN, 6 bd du Marechal Juin, 14050 Caen
Cedex 4, France

[‡] Institut Jean Lamour, UMR 7198, CNRS, Université de Lorraine, Faculté des Sciences et
Technologie, B.P. 70239, 54506 Vandœuvre-lès-Nancy Cedex, France

[#] Institut de Physique de Rennes, UMR UR1-CNRS 6251, Université de Rennes I, Campus de
Beaulieu, Bâtiment 11A, F-35042 Rennes Cedex, France

[§] Institut des Sciences Chimiques de Rennes (ISCR) - UMR CNRS 6226, Université de Rennes
I, Campus de Beaulieu, Bâtiment 10A, 35042 Rennes Cedex, France

KEYWORDS. thermoelectric, sulfide, stannoidite, mechanical alloying, SPS

ABSTRACT

A univalent copper hyper-stoichiometric stannoidite $\text{Cu}_{8+x}\text{Fe}_{3-x}\text{Sn}_2\text{S}_{12}$ with $0 \leq x \leq 0.5$ has been synthesized using mechanical alloying followed by spark plasma sintering. The X-ray diffraction analysis combined with ^{57}Fe and ^{119}Sn Mössbauer investigations has allowed the charge distribution of the cationic species on the various sites to be established and suggests the possibility of a small tin deficiency. The transport properties show a remarkable crossover from a semiconducting to a metal-like behaviour as the copper content increases from $x = 0$ to $x = 0.5$, whereas correlatively the Seebeck coefficient decreases moderately, with S values ranging from 310 to 100 $\mu\text{V}/\text{K}$. The thermal conductivity decreases as the temperature increases showing low values at high temperature, far below those reported in related stannite materials. The investigation of the thermoelectric properties shows that the ZT figure of merit is dramatically enhanced by the copper hyper-stoichiometry by a factor of 5 going from 0.07 for $x = 0$ to 0.35 for $x = 0.5$ at 630 K. This thermoelectric behaviour is interpreted on the basis of a model involving the Cu-S framework as the conducting electronic network where the $\text{Fe}^{2+}/\text{Fe}^{3+}$ species play the role of hole reservoir.

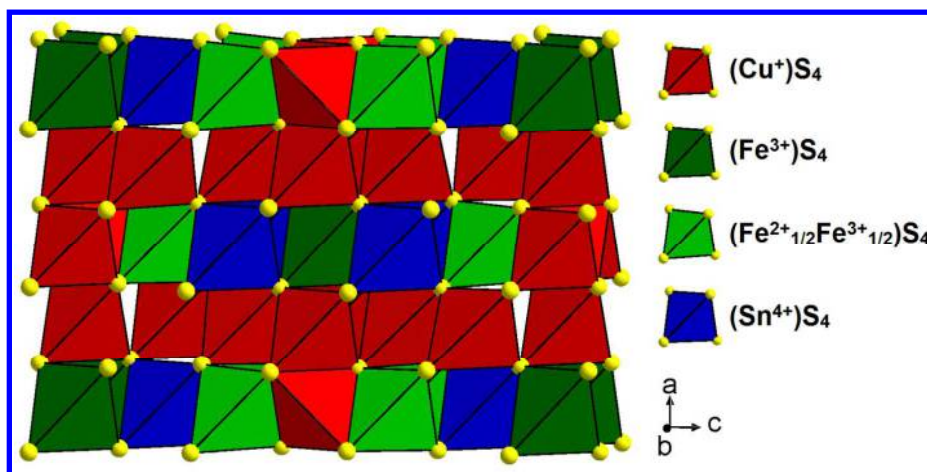
1. INTRODUCTION

The demand in energy consumption has been escalating this last decade, leading to renewed interest on thermoelectric (TE) technology.¹ Beyond the promising results obtained for telluride based materials which exhibit high performances,²⁻⁴ the need to conciliate efficiency with environmental and cost constraints has triggered research recently toward copper-based sulfides which have, for most of them, the advantage to contain eco-friendly and abundant elements. The figure of merit ZT values ($ZT = S^2T/\rho\kappa$, where S is the Seebeck coefficient, T is the absolute

1
2
3 temperature, ρ is the electrical resistivity and κ is the thermal conductivity) observed for the
4
5 simple phases Cu_{2-x}S , ranging from 0.5 to 1.7⁵⁻⁷ are very attractive. However, the electro-
6
7 migration of copper that appears in the Cu-S system weakens the stability and durability of these
8
9 TE materials. The introduction of other metallic (M) elements besides copper has allowed this
10
11 problem to be mostly overcome, opening the route to the exploration of complex copper based
12
13 sulfides. Actually, from the viewpoint of thermoelectricity, two classes of copper based sulfides
14
15 can be distinguished exhibiting an n-type and p-type conductivity, respectively. The n-type class
16
17 is obtained for lower copper content materials, *i.e.* Cu/M ratio ≤ 1 , as shown for chalcopyrite
18
19 CuFeS_2 -type sulfides such as $\text{CuFe}_{1-x}\text{In}_x\text{S}_2$ ⁸ and $\text{Cu}_{1-x}\text{Zn}_x\text{FeS}_2$ ⁹ and for the cubic isocubanite
20
21 CuFe_2S_3 ¹⁰, suggesting that the Fe 3d states play a major role in the formation of the electronic
22
23 band structure of these n-type thermoelectrics. The p-type class of copper based sulfides covers a
24
25 broad range of compositions, from Cu/M ratio equal or close to 1 as exemplified by the stannites
26
27 Cu_2ZnXS_4 (X=Sn, Ge)^{11,12} and copper-rich sulfides, with Cu/M ratios ranging from 2 to 5 as
28
29 shown by Cu_2SnS_3 ,¹³ the derivatives of the tetrahedrite $\text{Cu}_{12}\text{Sb}_4\text{S}_{13}$,¹⁴⁻¹⁶ of the colusite
30
31 $\text{Cu}_{26}\text{V}_2\text{Sn}_6\text{S}_{32}$,¹⁷⁻¹⁹ and of the bornite Cu_5FeS_4 .²⁰⁻²²

32
33
34 From these studies, the p-type copper rich sulfides appear as most promising for thermoelectric
35
36 applications. However, the improvement of the thermoelectric performances of these materials
37
38 remains a challenge, due to the interdependent and contrary effects of their electrical and thermal
39
40 transport parameters S , ρ and κ . The nature of the chemical bonds, especially Cu-S bonds and of
41
42 the distribution of charges in these complex structures is still a matter of debate, which is of
43
44 capital importance for the optimization of their TE properties. In this respect, the stannoidite
45
46 $\text{Cu}_8(\text{Fe,Zn})_3\text{Sn}_2\text{S}_{12}$ mineral appears to be an attractive material in relation with (i) its
47
48 orthorhombic structure²³ (Figure 1) closely related to that of stannite, (ii) the possibility to
49
50
51
52
53
54
55
56
57
58
59
60

1
2
3 prepare the synthetic isostructural $\text{Cu}_8\text{Fe}_3\text{Sn}_2\text{S}_{12}$ sulfide,²⁴ and (iii) the distribution of the cationic
4 charges according to the formula $(\text{Cu}^+)_8(\text{Fe}^{2+})(\text{Fe}^{3+})_2(\text{Sn}^{4+})_2(\text{S}^{2-})_{12}$ determined by Mössbauer
5 spectroscopy.²⁵ Curiously, the thermoelectric properties of this sulfide have not been investigated
6 to date, in spite of its potential to be used as a well characterized model material for
7 understanding the TE phenomena in these materials. We report herein on the synthesis by
8 mechanical alloying followed by spark plasma sintering (SPS) and on the TE properties of the
9 copper hyper-stoichiometric stannoidite $\text{Cu}_{8+x}\text{Fe}_{3-x}\text{Sn}_2\text{S}_{12}$ ($x \leq 0.5$) series. A drastic change in the
10 TE properties is observed with the copper content, characterized by a crossover from a
11 semiconducting poor TE ($ZT_{630\text{ K}} = 0.07$) state for the stoichiometric phase ($x = 0$) to a metallic-
12 like attractive TE ($ZT_{630\text{ K}} = 0.35$) state for the Cu-hyper-stoichiometric sulfide ($x = 0.5$). The
13 modification of these performances is explained in the frame of the iono-covalent model of the
14 chemical bonds.
15
16
17
18
19
20
21
22
23
24
25
26
27
28
29
30
31
32
33



50 Figure 1. View of the crystal structure of stannoidite $\text{Cu}_8\text{Fe}_3\text{Sn}_2\text{S}_{12}$.

51 52 53 54 55 2. EXPERIMENTAL SECTION

1
2
3 Polycrystalline samples of $\text{Cu}_{8+x}\text{Fe}_{3-x}\text{Sn}_2\text{S}_{12}$ ($0 \leq x \leq 0.5$) were synthesized by mechanical
4 alloying²⁶ followed by Spark Plasma Sintering. All sample preparation and handling of powders
5 were performed in Argon filled glove box with oxygen content of < 1 ppm. Stoichiometric
6 amounts of Cu (99.9 %, Alfa Aesar), Fe (99.9 %, Alfa Aesar), Sn (99.9 %, Alfa Aesar) and S
7 (99.99 %, Alfa Aesar) were loaded in a 25 ml tungsten carbide jar under argon atmosphere. The
8 powders were then milled in a high-energy planetary ball mill (Fritsch Pulverisette 7 Premium
9 line) at a speed of 600 rpm for 12 hours. The resulting powders were then ground and sieved
10 down to 150 μm . Powders were then placed in tungsten carbide dies of 10 mm diameter and
11 densified by Spark Plasma Sintering (SPS – FCT HPD 25) at 873 K for 15 min under a pressure
12 of 150 MPa (heating and cooling rate of 50 K/min and 20 K/min, respectively). This produced 10
13 mm diameter pellets, *ca.* 7 mm thick, with geometrical densities greater than 98 %. It is worth
14 pointing out that these samples are air sensitive and contain small traces of SnO_2 .
15
16
17
18
19
20
21
22
23
24
25
26
27
28
29
30

31 The crystalline phases were identified at room temperature by powder X-ray diffraction
32 (PXRD) using a X'Pert Pro PANalytical diffractometer using $\text{Co K}\alpha$ radiation ($\lambda = 1.78901 \text{ \AA}$).
33 Data were collected over the angular range $5 \leq 2\theta/^\circ \leq 100$ with a step size of 0.0131° and a step
34 time of 250 s, using a rotating sample holder in order to increase accuracy of the measurements.
35 Rietveld refinements from data collected on the sintered samples have been performed using
36 FullProf and WinPlotr software packages.^{27,28}
37
38
39
40
41
42
43
44
45

46 Seebeck coefficient and electrical resistivity were measured under helium atmosphere using
47 steady state technique and four probe method, respectively, (ZEM-3, ULVAC-RIKO, Japan)
48 over the temperature range of 300 K to 650 K on a $9 \times 3 \times 3 \text{ mm}^3$ sample. The thermal diffusivity
49 (D) of a square sample ($6 \times 6 \times 1 \text{ mm}^3$) was measured from 300 K to 650 K in an inert atmosphere
50 using a Netzsch LFA457 apparatus. Heat capacity (C_p) was calculated using Dulong-Petit
51
52
53
54
55
56
57
58
59
60

1
2
3 approximation. Thermal conductivity (κ) was calculated from the product of the sample density
4 (d), thermal diffusivity (D) and heat capacity (C_p). The combined uncertainty in the
5
6 determination of the ZT values is estimated to be 17%.²⁹
7
8

9
10 Room temperature Hall effect measurements were carried out using Physical Properties
11 Measurement System (PPMS; Quantum Design) under an applied magnetic field up to 9T.
12
13 However, it is difficult to extract reliable carrier concentrations from the Hall effect data since
14
15 the samples are magnetic and the contribution of the anomalous Hall effect appears to be
16
17 significant. Attempts to calculate the carrier concentration using the approximation of single
18
19 parabolic band conduction model, using the formula $p = 1/R_H \cdot e$, where e is the electronic charge;
20
21 gives an unrealistically high value of $p = 7.8 \times 10^{19} \text{ cm}^{-3}$, suggesting a very strong anomalous
22
23 contribution. Values for $x = 0.3$ and $x = 0.5$ appear to be more reasonable but could be
24
25 overestimated ($p = 1.2 \times 10^{22} \text{ cm}^{-3}$ and $1.1 \times 10^{22} \text{ cm}^{-3}$). Due to the linearity of the Hall signal with
26
27 magnetic field, it is nevertheless difficult to account for the anomalous contribution. Another
28
29 possibility is that two types of carrier are present, which could also cause the carrier
30
31 concentration to be overestimated. Low temperature or very high magnetic field studies are
32
33 required to confirm which effect is relevant.
34
35
36
37
38
39
40
41

42 ⁵⁷Fe and ¹¹⁹Sn Mössbauer spectra were measured at $T = 300 \text{ K}$ in transmission geometry
43
44 with a spectrometer operated in the conventional constant-acceleration mode. Some ⁵⁷Fe spectra
45
46 were recorded at 80 K thanks to a JANIS (*research company inc.*) liquid helium cryostat.
47
48 Polycrystalline absorbers, with natural abundance of ⁵⁷Fe or ¹¹⁹Sn isotope and thickness of ~ 15
49
50 mg cm^{-2} , were used. Sources were kept at room temperature (RT) to collect either ⁵⁷Fe or ¹¹⁹Sn
51
52 Mössbauer spectra. For ⁵⁷Fe spectra, the source was ⁵⁷Co in Rh matrix with a nominal strength of
53
54 25 mCi. For ¹¹⁹Sn spectra, the source was Ba^{119m}SnO₃ with a nominal strength of 10 mCi. A
55
56
57
58
59
60

1
2
3 palladium foil of 0.5 mm thickness was used as a critical absorber for tin X-rays. Velocity
4
5 calibration was performed against a 12 μm -thick $\alpha\text{-Fe}$ foil at RT . ^{57}Fe and ^{119}Sn isomer shifts (δ)
6
7 are referred respectively to $\alpha\text{-Fe}$ and to BaSnO_3 at RT . Mössbauer spectra were fitted with a
8
9 least-squares method program assuming Lorentzian peaks.
10
11

12 13 14 15 **3. RESULTS AND DISCUSSION**

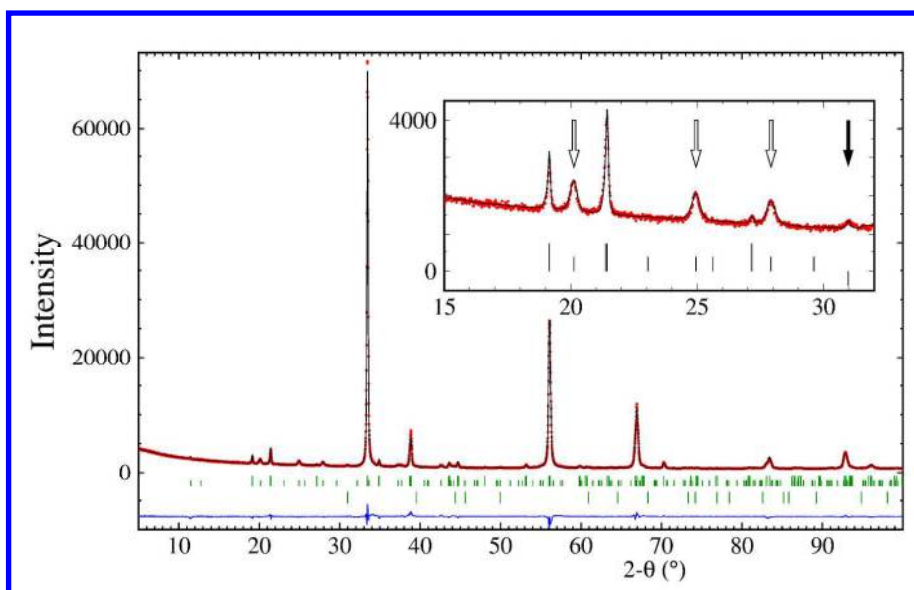
16 17 18 **3.1. Structural Analysis**

19
20 High-energy ball-milling of elemental powder mixture with stoichiometry ranging from
21
22 $\text{Cu}_8\text{Fe}_3\text{Sn}_2\text{S}_{12}$ to $\text{Cu}_{8.5}\text{Fe}_{2.5}\text{Sn}_2\text{S}_{12}$ produces fine black powders. Typical X-ray powder diffraction
23
24 pattern of these samples is presented in Figure S1. Then, SPS performed at 873 K on the seven
25
26 $\text{Cu}_{8+x}\text{Fe}_{3-x}\text{Sn}_2\text{S}_{12}$ samples, not only leads to compact pellets, but also allows to obtain highly pure
27
28 and well-crystallized stannoidite samples. This synthesis process was previously proved to be
29
30 efficient to prepare large quantity of high purity samples of other ternary and quaternary
31
32 sulfides.^{18,22,30–32} The PXRD pattern of $x = 0$ (Figure 2) and $x = 0.3$ samples (Figure S2) are
33
34 characteristic of the stannoidite structure and could be indexed in an orthorhombic unit-cell with
35
36 the space group $I222$. Our unit-cell parameters for $x = 0$ sample ($a = 10.758(1)$ Å; $b = 5.3971(2)$
37
38 Å; $c = 16.135(2)$ Å, Table S1) are also comparable with those previously reported for natural
39
40 stannoidite minerals, and present only small deviations due to slightly different chemical
41
42 compositions. As shown by previous studies,^{23,25} the crystal structure of stannoidite is closely
43
44 related to that of stannite. A blow up of the low intensity region from 17° to 32° , (insets Figure 2
45
46 and S2), shows the superstructure diffraction peaks of the stannoidite with respect to the stannite
47
48 phase ($I-42m$). These superstructure reflections, indexed with $h,k,l = 3n+1$ and $h,k,l = 3n+2$, are
49
50 broadened with respect to the main reflections, indexed with $h,k,l = 3n$. This broadening of the
51
52
53
54
55
56
57
58
59
60

1
2
3
4
5
6
7
8
9
10
11
12
13
14
15
16
17
18
19
20
21
22
23
24
25
26
27
28
29
30
31
32
33
34
35
36
37
38
39
40
41
42
43
44
45
46
47
48
49
50
51
52
53
54
55
56
57
58
59
60

superstructure reflections may indicate presence of atomic disorder or crystallographic defects. For the Rietveld refinements from PXRD data, the occupancy factors of the cationic sites were kept unchanged with respect to the mineral, since copper and iron cannot be distinguished one from the other from XRPD data due to their very close atomic numbers. From these refinements, the overall B factor converged to a reasonable value ($B = 0.78(8) \text{ \AA}^2$ for $x = 0$). This supports that the existing cationic disordering is limited. The refined atomic coordinates, cell parameters and reliability factors for $x = 0$ and $x = 0.3$ are listed in Table S1 and S2. It is worth pointing out that the cell parameters decrease as x increases, *i.e.* as Fe^{2+} is replaced by the couple $\text{Fe}^{3+}/\text{Cu}^+$, in agreement with the size of the metallic cations.

These first results attest that the crystallographic structure of these synthetic sulfides is equivalent to that previously described by Kudoh and Takeuchi²³ for the mineral stannoidite and consists of edge-sharing CuS_4 , SnS_4 and FeS_4 ordered tetrahedra, where metallic atoms are distributed on seven different crystallographic sites. Thus the structure of stoichiometric $\text{Cu}_8\text{Fe}_3\text{Sn}_2\text{S}_{12}$ (Figure 1) can be described as the stacking along the a axis of pure tetrahedral univalent copper layers alternating with mixed tetrahedral layers containing copper, tin and iron.



1
2
3 Figure 2. Rietveld refinement of $\text{Cu}_8\text{Fe}_3\text{Sn}_2\text{S}_{12}$: as usual, red dots, black and blue curves
4 represent the observed, calculated and difference plots, respectively. The green vertical lines
5 represent the position of the Bragg reflections. Top lines are reflections of the stannoidite: short
6 lines are $h,k,l=3n+1$ and $h,k,l=3n+2$ reflections while large lines are $h,k,l=3n$ reflections.
7 Bottom lines are reflections of the SnO_2 impurity. The inset shows the broadening of the h,k,l
8 reflections with $l=3n+1$ and $l=3n+2$ (white arrows) and the main reflection of the SnO_2 impurity
9 ($< 1\%$ wt., black arrow).
10
11
12
13
14
15
16
17
18
19
20
21
22

23 3.2. Mössbauer Spectroscopy Characterizations

24 We performed a Mössbauer study of copper hyper stoichiometric sulfides $\text{Cu}_{8+x}\text{Fe}_{3-x}\text{Sn}_2\text{S}_{12}$ for x
25 = 0, 0.3 and 0.5 to follow the evolution of charge distributions with x . The ^{119}Sn RT Mössbauer
26 spectra of all three samples evidence only a narrow quadrupolar doublet, with a full width at half
27 maximum (FWHM) of $\sim 0.9 \text{ mm}\cdot\text{s}^{-1}$, an isomer shift $\text{IS} = 1.42 \pm 0.02 \text{ mm}\cdot\text{s}^{-1}$ and a quadrupole
28 splitting (QS) of $0.42 \pm 0.02 \text{ mm}\cdot\text{s}^{-1}$. This isomer shift value is characteristic of tin atoms in a
29 +IV oxidation state, in fair agreement with the one, $1.48 \pm 0.05 \text{ mm}\cdot\text{s}^{-1}$ reported for
30 $\text{Cu}_8\text{Fe}_3\text{Sn}_2\text{S}_{12}$.²⁵ Yamanaka and Kato emphasize that ^{119}Sn isomer shifts in stannite
31 $\text{Cu}_2(\text{Fe,Zn})\text{SnS}_4$ ($\text{Zn/Fe}=0.3$), stannoidite $\text{Cu}_8(\text{Fe,Zn})_3\text{Sn}_2\text{S}_{12}$ ($\text{Zn/Fe}=0.07$), and mawsonite
32 $\text{Cu}_6\text{Fe}_2\text{SnS}_8$, which ranges from $1.45 \pm 0.03 \text{ mm}\cdot\text{s}^{-1}$ to $1.48 \pm 0.03 \text{ mm}\cdot\text{s}^{-1}$, support the
33 assumption of a strongly covalent SnS_4 -tetrahedron in these minerals. Similarly, the ^{119}Sn isomer
34 shift in the sulfide $\text{Cu}_2\text{FeSnS}_4$ ($(\text{Cu}^+)_2(\text{Fe}^{2+})(\text{Sn}^{4+})(\text{S}^{2-})_4$) is $\text{IS} = 1.48 \pm 0.03 \text{ mm}\cdot\text{s}^{-1}$.³³ We
35 conclude finally that the aforementioned isomer shifts are consistent with typical values, ~ 1.3
36 $\text{mm}\cdot\text{s}^{-1}$, obtained for tetrahedral Sn(IV)S_4 and discussed theoretically by Lippens.³⁴ A
37
38
39
40
41
42
43
44
45
46
47
48
49
50
51
52
53
54
55
56
57
58
59
60

representative ^{119}Sn Mössbauer spectrum is shown in Figure 3, where a small amount of SnO_2 (~2% of Sn atoms) is observed as explained in the experimental section.

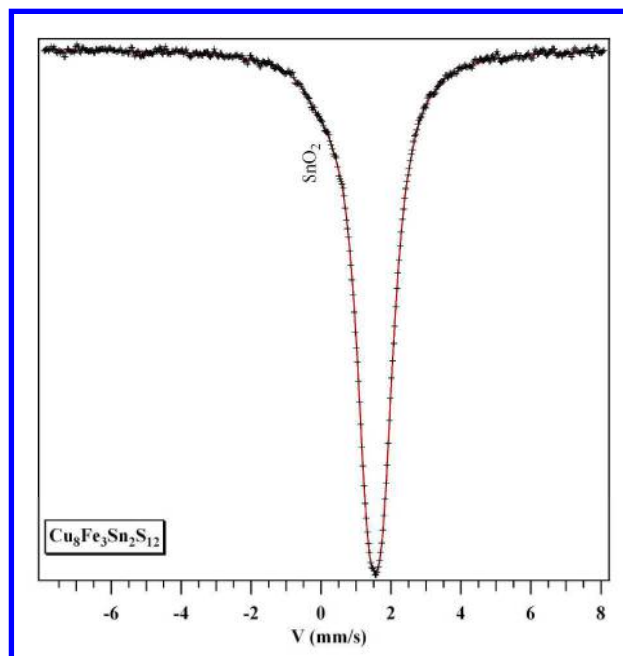


Figure 3. RT ^{119}Sn Mössbauer spectrum of $\text{Cu}_8\text{Fe}_3\text{Sn}_2\text{S}_{12}$

^{57}Fe Mössbauer spectra of $\text{Cu}_{8+x}\text{Fe}_{3-x}\text{Sn}_2\text{S}_{12}$ are shown in Figure 4a and 4b at 300K for $x = 0$, 0.3 and 0.5, and at 80 K for $x = 0$ and 0.3, respectively. Typical FWHM's range between ~ 0.25 $\text{mm}\cdot\text{s}^{-1}$ and 0.35 $\text{mm}\cdot\text{s}^{-1}$. Lamb-Mössbauer factors are needed to convert relative spectral areas of the various components of ^{57}Fe Mössbauer spectra into iron abundances. We assume that these factors have here similar values for Fe^{2+} and Fe^{3+} (see ref.²⁵) so that relative abundances coincide with relative areas. Hyperfine parameters and relative areas obtained from spectra fittings are given in Table 1 for $T = 80$ K and 300 K. The moderate temperature variation of the relative areas between 300K and 80K supports the above assumption.

An outer doublet with a large quadrupole splitting, $\text{QS} \sim 2.9$ $\text{mm}\cdot\text{s}^{-1}$ and an isomer shift $\text{IS} \sim 0.6$ $\text{mm}\cdot\text{s}^{-1}$ at RT is observed for $x < 0.5$ (Table 1). The latter is then attributed to Fe^{2+} .³⁵ Its

quadrupole splitting agrees with those reported by Yamanaka and Kato²⁵ for Fe²⁺ in stannoidite Cu₈(Fe,Zn)₃Sn₂S₁₂ (Zn/Fe = 0.3) and in Cu₈Fe₃Sn₂S₁₂, both being 2.86 ± 0.08 mm.s⁻¹. In addition, it is quite close to QS = 2.87 ± 0.03 mm.s⁻¹ measured for Fe²⁺ in Cu₂FeSnS₄ ((Cu⁺)₂(Fe²⁺)(Sn⁴⁺)(S²⁻)₄) by Eibschütz et al.³³

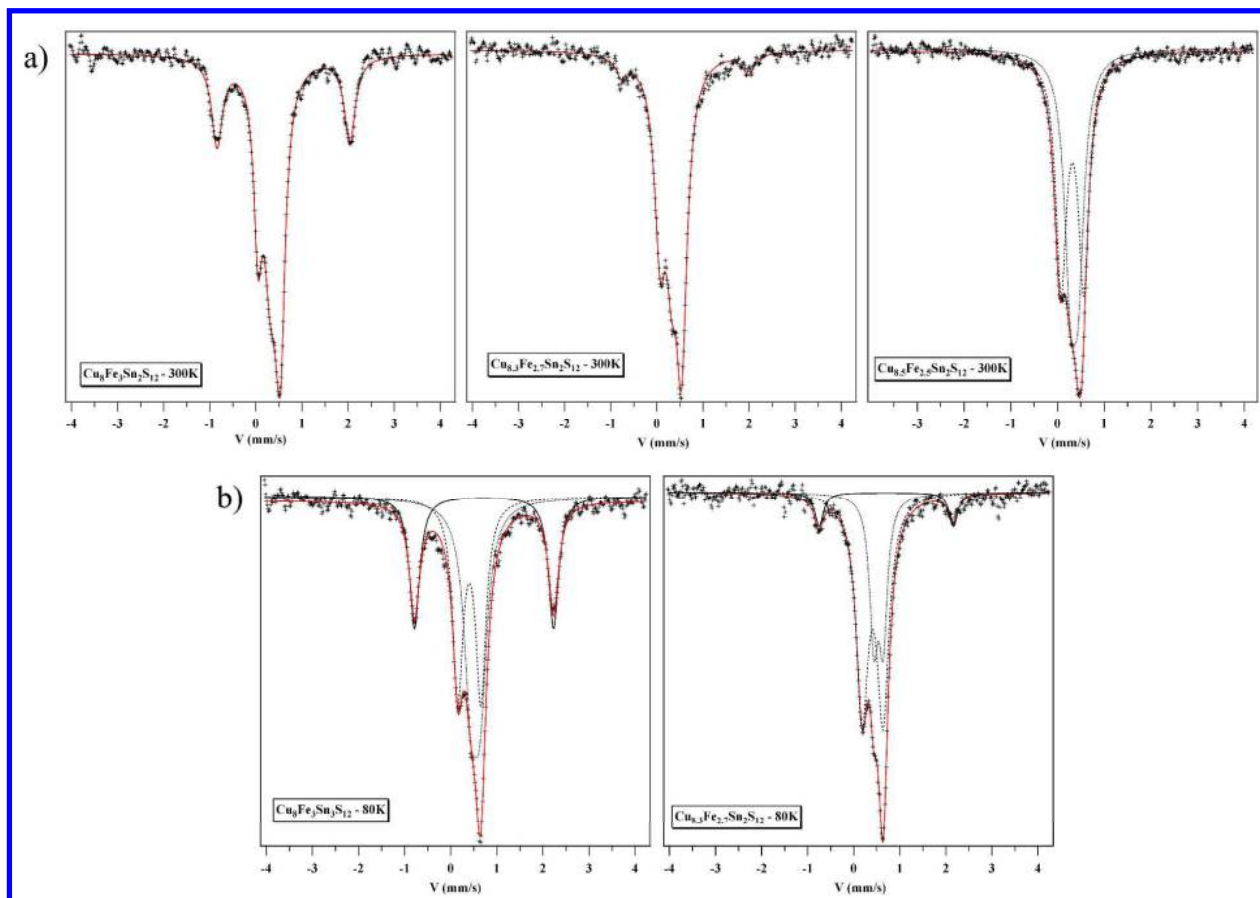


Figure 4. ⁵⁷Fe Mössbauer spectra of Cu_{8+x}Fe_{3-x}Sn₂S₁₂ with *x* increasing from left to right (a) top row, at 300 K for *x* = 0, 0.3 and 0.5 and b) bottom row, at 80 K for *x* = 0 and 0.3

When copper excess is substituted for iron in Cu₈Fe₃Sn₂S₁₂ to yield Cu_{8+x}Fe_{3-x}Sn₂S₁₂, the relative values of the redox potential of the Cu²⁺/Cu⁺ and Fe³⁺/Fe²⁺ couples favour the oxidation of Fe²⁺ by Cu²⁺ as the equilibrium Cu²⁺ + Fe²⁺ ⇌ Cu⁺ + Fe³⁺ (1) is strongly displaced toward the right. ⁵⁷Fe Mossbauer spectra of three samples with *x* = 0, 0.3 and 0.5 (Figure 4a) confirm that

1
2
3 the Fe^{2+} content decreases at the expense of the Fe^{3+} content (Table 1) as expected when copper
4 (Cu^+) substitutes for iron. Thus, from the viewpoint of major charges, the formula of a copper
5 hyper stoichiometric phase can be formally written as $(\text{Cu}^+)_{8+x}(\text{Fe}^{2+})_{1-2x}(\text{Fe}^{3+})_{2+x}(\text{Sn}^{4+})_2(\text{S}^{2-})_{12}$. As
6
7
8 a consequence, a Cu substitution limit is reached in $(\text{Cu}^+)_{8.5}(\text{Fe}^{3+})_{2.5}(\text{Sn}^{4+})_2(\text{S}^{2-})_{12}$ with $x = 0.50$, a
9
10
11 value for which the Fe^{2+} species is predicted to disappear in agreement with experimental results
12
13
14 (Figure 4a, $T = 300\text{K}$).

15
16
17 A first notable result is that the relative area of the Fe^{2+} component, called here $A^{2+}(x)$, is
18
19
20 clearly smaller than the one, $(1-2x)/(3-x)$, expected from the sulfide formula $(\text{Cu}^+)_{8+x}(\text{Fe}^{2+})_{1-2x}$
21
22
23 $(\text{Fe}^{3+})_{2+x}(\text{Sn}^{4+})_2(\text{S}^{2-})_{12}$ (Table 1) for $x = 0$ and 0.3 . These deviations can be explained by a small
24
25
26 deviation of the Sn content from the stoichiometric value of 2 as small amounts of tin dioxide are
27
28
29 observed on ^{119}Sn Mössbauer spectra (see for instance Figure 3). With the latter assumption, we
30
31
32 obtain the Sn content from the experimental values of $A^{2+}(x)$ values given in Table 1 and we get
33
34
35 $(\text{Cu}^+)_8(\text{Fe}^{2+})_{0.75}(\text{Fe}^{3+})_{2.25}(\text{Sn}^{4+})_{1.94}(\text{S}^{2-})_{12}$ and $(\text{Cu}^+)_{8.3}(\text{Fe}^{2+})_{0.18}(\text{Fe}^{3+})_{2.52}(\text{Sn}^{4+})_{1.94}(\text{S}^{2-})_{12}$ for $x = 0$
36
37
38 and $x = 0.3$ respectively. Interestingly, the Sn content deviates similarly from 2 in both cases,
39
40
41 namely by ~ 0.06 that we interpret by the existence of Sn vacancies. The amount of SnO_2
42
43
44 expected from this deviation is $\sim 3\%$ in agreement with the value observed for $x = 0$ (Figure 3).

45
46
47 The main feature of all ^{57}Fe spectra is a central component, which consists apparently of
48
49
50 two outer peaks and of an inner peak seen as a shoulder (Figure 4). The overall impression is that
51
52
53 this central component remains essentially unchanged when x varies. The latter component
54
55
56 includes actually two doublets, *i.e.* four peaks labelled from 1 to 4 from negative to positive
57
58
59 velocities. For $x = 0$, these four peaks have close areas so that two peak associations must be
60
61
62 considered, on the one hand (1-2) and (3-4), and (1-4) and (2-3) on the other. The RT spectrum
63
64
65 of $\text{Cu}_{8.5}\text{Fe}_{2.5}\text{Sn}_2\text{S}_{12}$ shows unambiguously that only the second is possible. From the hyperfine
66
67
68

parameters of Table 1, we are led to conclude that Fe^{3+} ions³⁵ give rise to two different doublets for any value of x . Their hyperfine parameters change little with x (Table 1).

Table 1: ^{57}Fe hyperfine parameters: isomer shifts (IS) and quadrupole splittings (QS) for the various sites of Mössbauer spectra at 300 K and at 80 K. The bracketed relative area given for Fe^{2+} is equal to $(1-2x)/(3-x)$.

T	Sulfides $\text{Cu}_{8+x}\text{Fe}_{3-x}\text{Sn}_2\text{S}_{12}$	Sites	300 K			80 K		
			IS mm.s^{-1} (± 0.03)	QS mm.s^{-1} (± 0.03)	Relative area % (± 3)	IS mm.s^{-1} (± 0.03)	EQ mm.s^{-1} (± 0.03)	Relative area % (± 3)
	$\text{Cu}_8\text{Fe}_3\text{Sn}_2\text{S}_{12}$ ($x = 0$)	Fe^{2+}	0.59	2.88	23 (33)	0.71	3.01	25 (33)
		$\text{Fe}^{3+}_{\text{I}}$	0.40	0.18	34	0.52	0.18	38
		$\text{Fe}^{3+}_{\text{II}}$	0.29	0.48	42	0.39	0.50	36
	$\text{Cu}_{8.3}\text{Fe}_{2.7}\text{Sn}_2\text{S}_{12}$ ($x = 0.3$)	Fe^{2+}	0.60	2.80	7 (15)	0.69	2.92	7 (15)
		$\text{Fe}^{3+}_{\text{I}}$	0.43	0.20	26	0.42	0.20	25
		$\text{Fe}^{3+}_{\text{II}}$	0.31	0.44	67	0.31	0.44	68
	$\text{Cu}_{8.5}\text{Fe}_{2.5}\text{Sn}_2\text{S}_{12}$ ($x = 0.5$)	$\text{Fe}^{3+}_{\text{I}}$	0.35	0.16	47			
		$\text{Fe}^{3+}_{\text{II}}$	0.29	0.48	53			

The assumption that Fe^{2+} and Fe^{3+} occupy respectively the 2(a) and 4(i) sites in $(\text{Cu}^+)_{8-x}(\text{Fe}^{2+})_x(\text{Fe}^{3+})_{2-x}(\text{Sn}^{4+})_2(\text{S}^{2-})_{12}$ is incompatible with the existence of two different Fe^{3+} components with almost equal abundances. We can then propose that site 2(a) is occupied by 1 Fe^{3+} ion while site 4(i) is occupied by 1 Fe^{2+} and 1 Fe^{3+} cations. A similar remark holds for the other samples. This implies that the excess Cu ions in the hyper stoichiometric compounds are located on the 4(i) site.

From bond lengths²³ and from Mössbauer hyperfine parameters²⁵ in the sulfide $\text{Cu}_8\text{Fe}_3\text{Sn}_2\text{S}_{12}$ ($x = 0$), it was concluded that the major cationic species are Cu^+ , Sn^{4+} , Fe^{3+} and Fe^{2+} which leads to write its formula as $(\text{Cu}^+)_{8-x}(\text{Fe}^{2+})_x(\text{Fe}^{3+})_{2-x}(\text{Sn}^{4+})_2(\text{S}^{2-})_{12}$ with an ordered distribution of Fe^{3+} and Fe^{2+} in the mixed layers. Yamanaka and Kato²⁵ reported that their ^{57}Fe Mössbauer spectra are composed of two Fe doublets with an outer one due to ferrous ions and an inner one due to ferric ions. The intensity of the inner doublet is mentioned to be twice that of the outer doublet,

1
2
3 assuming that ferrous and ferric ions have identical Lamb-Mössbauer factors. Figure 4 shows
4 outer “ferrous” doublets whose hyperfine parameters are similar to those reported by the latter
5
6
7
8 authors. However, the inner central components of our ^{57}Fe Mössbauer spectra consist of more
9
10
11 than one doublet and are satisfactorily fitted with two doublets. This conclusion is at variance
12
13 with the statements of Yamanaka and Kato²⁵. As the ^{57}Fe Mössbauer spectra and velocity range
14
15 information are not mentioned in their study, it is difficult to understand, if the inner component
16
17 that they discussed, consists actually of one doublet or more. The FWHM of the inner lines of
18
19 the bcc α -Fe spectrum is 0.30 mm.s^{-1} at room temperature in the study of Yamanaka and Kato
20
21 while it is 0.23 mm.s^{-1} in our case. Their conclusions might result from a lack of spectral
22
23 resolution. Differences in the preparation processes of the investigated sulfides might also
24
25 constitute an alternative explanation of the differences between ^{57}Fe Mössbauer spectra.
26
27

28
29 In summary, we conclude to the presence of small amounts of Sn vacancies in the investigated
30
31 sulfides. In addition, the repartition of Fe^{2+} and Fe^{3+} on the 2(a) and 4(i) sites is found to differ
32
33 from the classically assumed one.
34
35
36
37
38

39 **3.3. Thermoelectric properties**

40
41 The electrical resistivity plots versus temperature for the seven $\text{Cu}_{8+x}\text{Fe}_{3-x}\text{Sn}_2\text{S}_{12}$ compositions
42
43 (Figure 5a) clearly show a crossover from a semi-conducting to a metallic-like behaviour with a
44
45 decrease of the resistivity by almost three orders of magnitude at room temperature as the copper
46
47 content increases from $x = 0$ to $x = 0.50$. Indeed, $\text{Cu}_8\text{Fe}_3\text{Sn}_2\text{S}_{12}$ is a semi-conductor with a
48
49 resistivity of $745 \text{ m}\Omega \text{ cm}$ at room temperature, whereas the hyper stoichiometric phase
50
51 $\text{Cu}_{8.5}\text{Fe}_{2.5}\text{Sn}_2\text{S}_{12}$ evidences the best semi-metallic behaviour of the series with a resistivity of 2.75
52
53 $\text{m}\Omega \text{ cm}$ at room temperature. Moreover the evolution of the resistivity values is quite continuous,
54
55
56
57
58
59
60

1
2
3 the semi-conducting character decreasing regularly from $x = 0$ to $x = 0.5$, leaving place beyond x
4 = 0.3 to a metal-like behaviour. It is worth pointing out that copper hyper-stoichiometry was
5 already shown to be a promising way to bring down the resistivity over the pristine phase in
6 systems such as $\text{Cu}_{2+x}\text{Mg}_{1-x}\text{SnSe}_4$ and $\text{Cu}_{2+x}\text{Cd}_{1-x}\text{SnSe}_4$.^{36,37}
7
8

9
10 The evolution of the Seebeck coefficient versus temperature (Figure 5b) shows that they are all
11 p-type materials with rather high S values ranging from 310 to 100 $\mu\text{V}/\text{K}$ at room temperature.
12
13 As expected, the thermal evolution of S is closely related to that of ρ . Indeed, for $x \leq 0.22$, S
14 decreases as T increases, *i.e.* as ρ decreases, whereas for $x \geq 0.3$, the opposite is observed. A
15 nearly independent temperature behaviour for $x = 0.25$ is observed, suggesting that this chemical
16 composition is close to the semi-conductor to metal-like transition in this system. Note that the x
17 = 0.22 sample was synthesized in addition to the other samples to determine more precisely the
18 composition window where the transition occurs. Moreover, S decreases as x increases in
19 agreement with the crossover from the semiconducting to the metal-like behaviour observed
20 from electrical resistivity. For the pristine sulfide $\text{Cu}_8\text{Fe}_3\text{Sn}_2\text{S}_{12}$, the Seebeck coefficient also
21 decreases as T increases in agreement with its semiconducting behaviour. Nevertheless, the S
22 value of this compound is smaller than that of the semi-conducting $x = 0.10$ phase, in spite of its
23 higher resistivity.
24
25
26
27
28
29
30
31
32
33
34
35
36
37
38
39
40
41
42
43
44
45
46
47
48
49
50
51
52
53
54
55
56
57
58
59
60

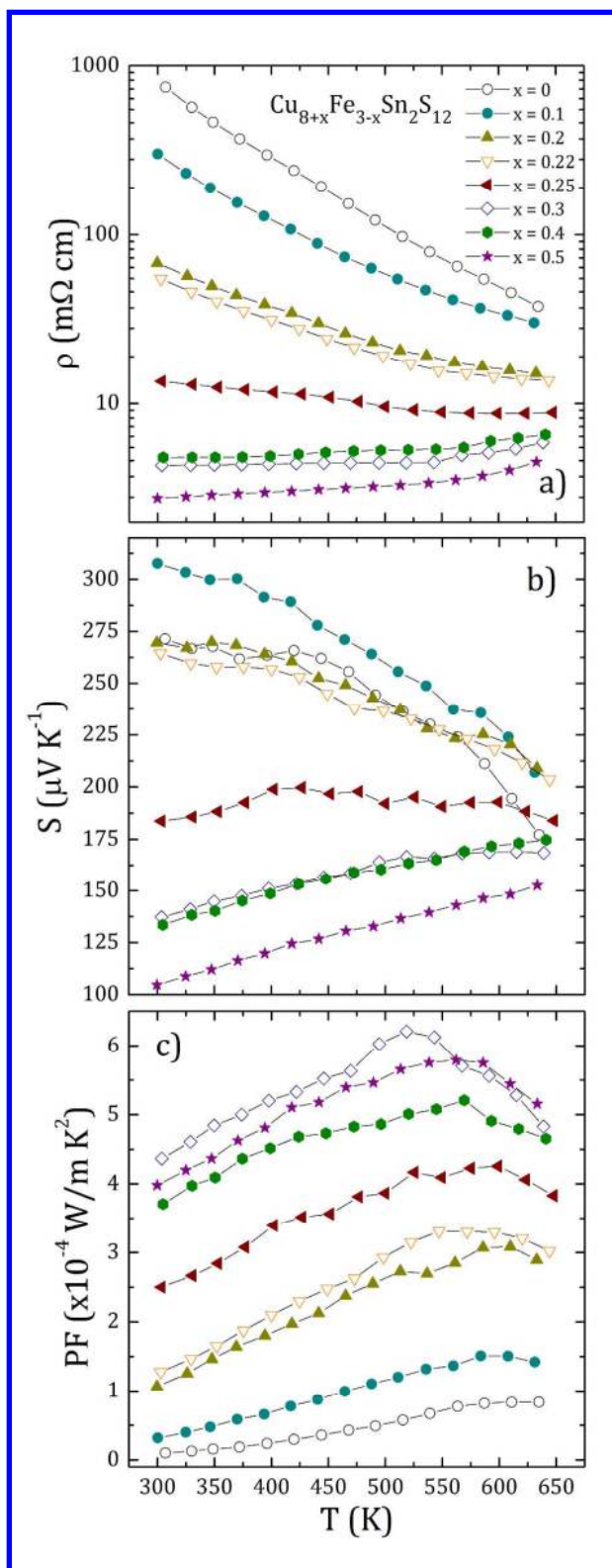


Figure 5. Temperature dependence of (a) electrical resistivity, (b) Seebeck coefficient and (c) power factor in the $\text{Cu}_{8+x}\text{Fe}_{3-x}\text{Sn}_2\text{S}_{12}$ series.

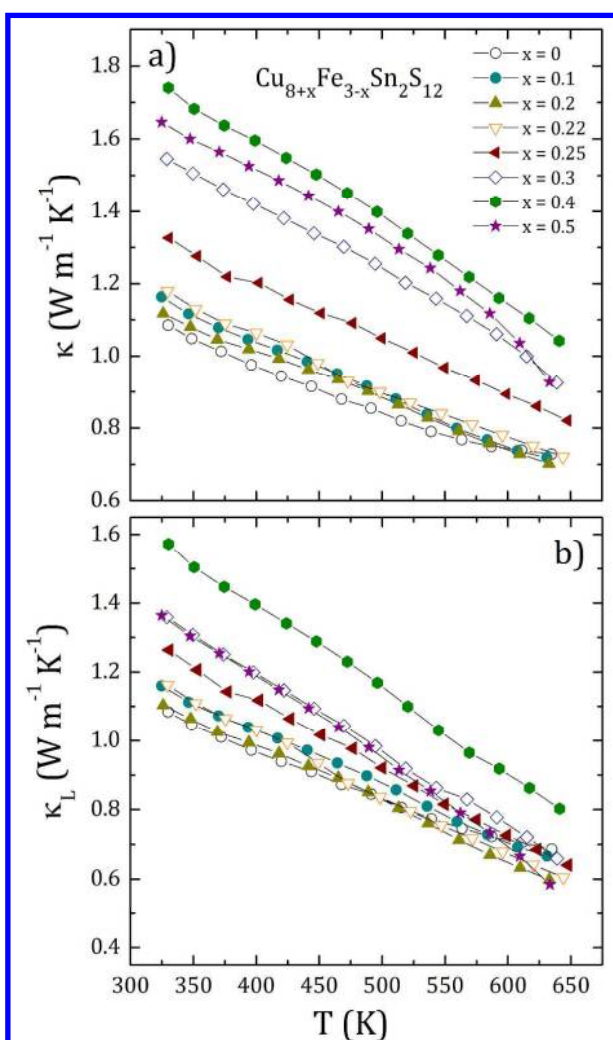
1
2
3 Considering that the Sn^{4+} cations cannot participate to the electrical conduction, due to the $4d^{10}$
4 nature of their orbitals, only Cu^+ , Fe^{2+} and Fe^{3+} should be involved in the electrical conductivity
5 of these materials. The high univalent copper content and the fact that the CuS_4 tetrahedra form a
6 3D-framework (Figure 1) strongly suggest that the p-type transport properties in this sulfide
7 material are governed by the Cu(I)-S framework involving a hybridization of the $\text{Cu}(3d^{10})$ and
8 $\text{S}(3p^4)$ orbitals. In this model, the presence of hole carriers in the copper network, *i.e.* the mixed
9 valence $\text{Cu}^{2+}/\text{Cu}^+$ is rigorously governed by the aforementioned equilibrium $\text{Cu}^{2+} + \text{Fe}^{2+} \rightleftharpoons \text{Cu}^+$
10 + Fe^{3+} (1). In other words, we believe that in this material, the Cu-S framework forms the
11 conducting electronic network, but that the $\text{Fe}^{3+}/\text{Fe}^{2+}$ species play the role of hole
12 donors/acceptors (reservoirs) for the generation and optimization of electrical properties.
13
14

15
16
17 Presence of large amount of Fe^{2+} , as in the stoichiometric compound $\text{Cu}_8\text{Fe}_3\text{Sn}_2\text{S}_{12}$, tends to
18 hinder the formation of Cu^{2+} centres (hole carriers) by the capture of the hole carriers to form
19 Fe^{3+} species according to the equation $\text{Fe}^{2+} + \text{h}^+ \rightarrow \text{Fe}^{3+}$ (2). This is in agreement with the
20 Vant'Hoff and Lechatelier law considering the equilibrium (1). Indeed, the latter imposes that
21 the presence of high Fe^{2+} content tends to displace the equilibrium in order to increase the Fe^{3+}
22 content, as already discussed above. Consequently, we expect that the formation of “mobile Cu^{2+}
23 centres” in the structure will be smaller for this limit composition, leading to a high resistivity
24 value, *i.e.* semi-conducting behaviour. For the hyper-stoichiometric sulfides $\text{Cu}_{8+x}\text{Fe}_{3-x}\text{Sn}_2\text{S}_{12}$, the
25 Fe^{2+} content is decreased continuously as x increases up to $x = 0.50$ and consequently the
26 equilibrium (1) tends to be displaced in the opposite direction. As a result, the content of Cu^{2+}
27 centres will tend to increase with x , leading to a metallic-like behaviour with the highest
28 electrical conductivity for higher x values. Note that additional hole carriers may also be created
29 by cationic deficiency as observed on the Sn site by Mössbauer spectroscopy.
30
31
32
33
34
35
36
37
38
39
40
41
42
43
44
45
46
47
48
49
50
51
52
53
54
55
56
57
58
59
60

1
2
3 Figure 5c represents the thermal evolution of the power factor in the $\text{Cu}_{8+x}\text{Fe}_{3-x}\text{Sn}_2\text{S}_{12}$ series.
4
5 The pristine $\text{Cu}_8\text{Fe}_3\text{Sn}_2\text{S}_{12}$ exhibits a PF value of $0.9 \times 10^{-5} \text{ W/m K}^2$ at 300 K, which increases to
6
7 $0.83 \times 10^{-4} \text{ W/m K}^2$ at 635 K. The increase of the copper concentration provides high power
8
9 factor, especially at higher temperatures, in relation with the decrease of the electrical resistivity.
10
11 As example, $\text{Cu}_{8.3}\text{Fe}_{2.7}\text{Sn}_2\text{S}_{12}$ sample exhibits a value of $4.36 \times 10^{-4} \text{ W/m K}^2$ at 300 K and reaches
12
13 a maximum of $6.2 \times 10^{-4} \text{ W/m K}^2$ at 520 K.
14
15
16
17

18 The temperature dependence of the total thermal conductivity is given in Figure 6a. All of
19
20 these materials present low κ values, ranging from 1.08 W/m K for $\text{Cu}_8\text{Fe}_3\text{Sn}_2\text{S}_{12}$ to 1.74 W/m K
21
22 for $\text{Cu}_{8.4}\text{Fe}_{2.6}\text{Sn}_2\text{S}_{12}$ at $T = 300\text{K}$. It is important to note that these low κ values are intrinsic to the
23
24 complex crystal structure of stannoidite and absolutely not a consequence of either poorly
25
26 densified samples (geometrical densities greater than 98 %) or of the presence of secondary
27
28 phases. For any copper content, the total thermal conductivity decreases monotonically with the
29
30 increase of the temperature, leading to very low κ values at high temperature ($\leq 1 \text{ W/m K}$). The
31
32 electronic contribution κ_e to the thermal conductivity is calculated using the Wiedemann-Franz
33
34 relation ($\kappa_e = L_0 \sigma T$), while the lattice thermal conductivity κ_L is obtained after subtracting κ_e
35
36 from κ , according to the relation $\kappa = \kappa_e + \kappa_L$. Figure 6b clearly shows that the lattice contribution
37
38 to the thermal conductivity is dominant over the entire measured temperature range, even if it
39
40 decreases monotonically when the temperature increases. As example, the κ_L value of the pristine
41
42 phase decreases from 1.1 W/m K at 325 K to 0.68 W/m K at 635 K. This suggests that the
43
44 decrease of the κ_L component is due to the increase of phonon-phonon scattering (Umklapp
45
46 process). Such low lattice thermal conductivity values observed in this stannoidite phase could
47
48 be due to mass contrast between $\text{Fe}^{2+}/\text{Fe}^{3+}$ and Cu^+ with Sn^{4+} along with other effects such as
49
50 those of point defects and strains. On the other hand, it is found that κ_L increases with x . This
51
52
53
54
55
56
57
58
59
60

1
2
3 may be due to the progressive disappearance of the mixed valence $\text{Fe}^{2+}/\text{Fe}^{3+}$ on the Fe
4
5 crystallographic sites when the copper concentration increases (*i.e.* decrease of the $\text{Fe}^{2+}/\text{Fe}^{3+}$
6
7 ratio from 1/2 in the pristine stannoidite to 0 for $x = 0.5$), which reduces the structural disorder in
8
9 the lattice. Finally, it must be pointed out that the κ_L values in the full series are also far below
10
11 from those reported in related-stannite compounds (for example, $\kappa_L = 4.7$ W/m K at RT in
12
13 $\text{Cu}_2\text{ZnSnS}_4$).¹¹ Remarkably, it is in the same range as other copper based sulfide minerals such as
14
15 pristine $\text{Cu}_{12}\text{Sb}_4\text{S}_{13}$ tetrahedrite¹⁵ and $\text{Cu}_{26}\text{V}_2\text{Sn}_6\text{S}_{32}$ colusite.^{18,38}
16
17
18
19



20
21
22
23
24
25
26
27
28
29
30
31
32
33
34
35
36
37
38
39
40
41
42
43
44
45
46
47
48
49
50
51
52
53 Figure 6. Temperature dependence of (a) total thermal conductivity and (b) lattice thermal
54
55 conductivity in the $\text{Cu}_{8+x}\text{Fe}_{3-x}\text{Sn}_2\text{S}_{12}$ series.
56
57
58
59
60

The dimensionless thermoelectric figure of merit ZT versus temperature is shown in Figure 7. Copper to iron substitution significantly enhances the thermoelectric performance of stannoidite, leading to a maximum ZT value of 0.35 at 630 K for the copper hyper-stoichiometric sample $x = 0.5$. The improvement here is nearly five fold over the pristine phase ($ZT = 0.07$ at 630 K). Such significant improvement in ZT is mainly associated to the semi-conducting to metal-like behaviour crossover induced by copper hyper-stoichiometry and to the very low thermal conductivity of these materials, especially at high temperature.

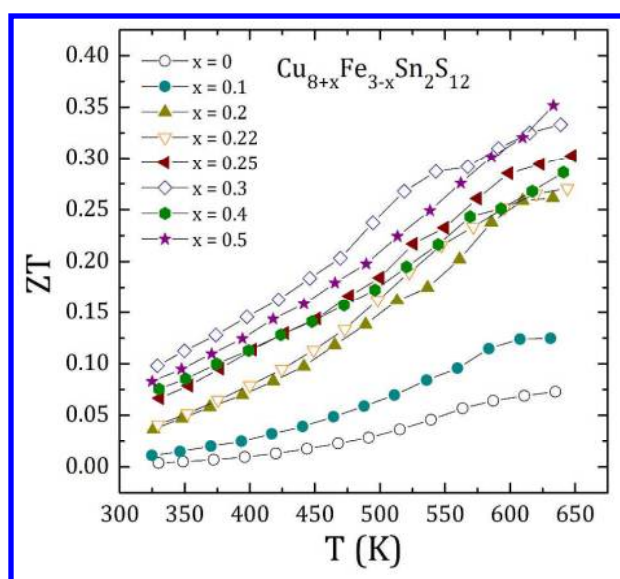


Figure 7. Temperature dependence of the figure of merit ZT in the $\text{Cu}_{8+x}\text{Fe}_{3-x}\text{Sn}_2\text{S}_{12}$ series.

4. CONCLUSION

We have demonstrated that high purity and compact $\text{Cu}_{8+x}\text{Fe}_{3-x}\text{Sn}_2\text{S}_{12}$ stannoidite bulk samples can be synthesized using mechanical alloying combined with spark plasma sintering. Besides the low cost and non-toxicity of the elements, this sulfide presents the advantage of a great flexibility for the optimization of its transport properties, by the control of the Cu content. Indeed, we have

1
2
3 shown that copper hyper-stoichiometry in stannoidite induces a drastic modification of its TE
4 properties from a semiconducting poor TE ($ZT_{630\text{ K}} = 0.07$) state for the pristine phase ($x = 0$) to a
5 semi-metallic attractive TE ($ZT_{630\text{ K}} = 0.35$) state for the richest copper phase ($x = 0.5$). The
6 optimization of these performances is explained in the frame of the iono-covalent model of the
7 chemical bonds, by varying the $\text{Fe}^{2+}/\text{Fe}^{3+}$ ratio leading to a semi-metallic behaviour with the
8 highest conductivity for higher x values. We have also shown that the thermal conductivity of
9 these stannoidite compounds is relatively low due to its complex crystal structure with a large
10 number of atoms in the unit cell and cationic sites. Moreover, even though the intrinsic
11 substitution allows a huge improvement in the ZT value over the pristine phase, it does not bring
12 reduction in the lattice thermal conductivity, leaving large possibilities for further enhancements
13 of the thermoelectric properties of stannoidite material by suitable substitutions.
14
15
16
17
18
19
20
21
22
23
24
25
26
27
28

29 We strongly believe that ternary/quaternary sulfides have to be more carefully investigated and
30 revisited by controlling accurately the effect of doping upon their electrical and thermal
31 properties, and developing innovative processes for reaching higher ZT values.
32
33
34
35

36 Additional Note: At the end of this study, we learned of that a stannoidite type material with the
37 only formula $\text{Cu}_{16}\text{Fe}_{4.3}\text{S}_{24}\text{Sn}_4\text{Zn}_{1.7}$ was revealed to exhibit thermoelectric properties with a ZT
38 factor of 0.22 at 623 K,³⁹ supporting the great potential of this structural type for thermoelectric
39 properties.
40
41
42
43
44
45
46
47
48
49
50
51
52
53
54
55
56
57
58
59
60

1
2
3 ASSOCIATED CONTENT
45
6
7 **Supporting Information.**
89
10 The following files are available free of charge.
1112 XRD pattern of ball-milled $\text{Cu}_8\text{Fe}_3\text{Sn}_2\text{S}_{12}$ powder (Figure S1, PDF)
1314 Rietveld refinement of XRD pattern of $\text{Cu}_{8.3}\text{Fe}_{2.7}\text{Sn}_2\text{S}_{12}$ (Figure S2, PDF)
1516
17 Crystallographic data for $\text{Cu}_{8-x}\text{Fe}_{3+x}\text{Sn}_2\text{S}_{12}$ (Table S1, PDF)
1819
20 Atomic coordinates for $\text{Cu}_{8-x}\text{Fe}_{3+x}\text{Sn}_2\text{S}_{12}$ (Table S2, PDF)
21
22
2324 AUTHOR INFORMATION
2526
27 **Corresponding Author**
2829
30 *E-mail: emmanuel.guilmeau@ensicaen.fr
31
3233 ACKNOWLEDGMENT
3435
36 The authors would like to thank Christelle Bilot and Jérôme Lecourt for technical support and
37
38 the financial support of the French Agence Nationale de la Recherche (ANR), through the
39
40 program “Investissements d’Avenir” (ANR-10-LABX-09-01), LabEx EMC3.
41
42
43
44
45
46
47
48
49
50
51
52
53
54
55
56
57
58
59
60

REFERENCES

- (1) Bell, L. E. Cooling, Heating, Generating Power, and Recovering Waste Heat with Thermoelectric Systems. *Science (80-.)*. **2008**, *321*, 1457–1461.
- (2) Pei, Y.; Shi, X.; LaLonde, A.; Wang, H.; Chen, L.; Snyder, G. J. Convergence of Electronic Bands for High Performance Bulk Thermoelectrics. *Nature* **2011**, *473*, 66–69.
- (3) Sootsman, J. R.; Chung, D. Y.; Kanatzidis, M. G. New and Old Concepts in Thermoelectric Materials. *Angew. Chemie - Int. Ed.* **2009**, *48*, 8616–8639.
- (4) Hsu, K. F.; Loo, S.; Guo, F.; Chen, W.; Dyck, J. S.; Uher, C.; Hogan, T.; Polychroniadis, E. K.; Kanatzidis, M. G. Cubic $\text{AgPb}_m\text{SbTe}_{2+m}$ Bulk Thermoelectric Materials with High Figure of Merit. *Science* **2004**, *303*, 818–821.
- (5) Liu, H.; Shi, X.; Xu, F.; Zhang, L.; Zhang, W.; Chen, L.; Li, Q.; Uher, C.; Day, T.; Snyder, G. J. Copper Ion Liquid-like Thermoelectrics. *Nat Mater* **2012**, *11*, 422–425.
- (6) Ge, Z.; Zhang, B.; Chen, Y.; Yu, Z.; Liu, Y.; Li, J.-F. Synthesis and Transport Property of $\text{Cu}_{1.8}\text{S}$ as a Promising Thermoelectric Compound. *Chem. Commun.* **2011**, *47*, 12697–12699.
- (7) He, Y.; Day, T.; Zhang, T.; Liu, H.; Shi, X.; Chen, L.; Snyder, G. J. High Thermoelectric Performance in Non-Toxic Earth-Abundant Copper Sulfide. *Adv. Mater.* **2014**, *26*, 3974–3978.
- (8) Xie, H.; Su, X.; Zheng, G.; Yan, Y.; Liu, W.; Tang, H.; Kanatzidis, M. G.; Uher, C.; Tang,

- 1
2
3 X. Nonmagnetic In Substituted $\text{CuFe}_{1-x}\text{In}_x\text{S}_2$ Solid Solution Thermoelectric. *J. Phys.*
4
5 *Chem. C* **2016**, *120*, 27895–27902.
6
7
8
9 (9) Xie, H.; Su, X.; Zheng, G.; Zhu, T.; Yin, K.; Yan, Y.; Uher, C.; Kanatzidis, M. G.; Tang,
10
11 X. The Role of Zn in Chalcopyrite CuFeS_2 : Enhanced Thermoelectric Properties of Cu_{1-x}
12
13 Zn_xFeS_2 with In Situ Nanoprecipitates. *Adv. Energy Mater.* **2017**, *7*, 1601299.
14
15
16
17 (10) Barbier, T.; Berthebaud, D.; Frésard, R.; Lebedev, O. I.; Guilmeau, E.; Eyert, V.;
18
19 Maignan, A. Structural and Thermoelectric Properties of N-Type Isocubanite CuFe_2S_3 .
20
21 *Inorg. Chem. Front.* **2017**, *4*, 424.
22
23
24
25 (11) Liu, M. L.; Huang, F. Q.; Chen, L. D.; Chen, I. W. A Wide-Band-Gap P-Type
26
27 Thermoelectric Material Based on Quaternary Chalcogenides of $\text{Cu}_2\text{ZnSnQ}_4$ (Q=S,Se).
28
29 *Appl. Phys. Lett.* **2009**, *94*, 202103.
30
31
32
33 (12) Heinrich, C. P.; Day, T. W.; Zeier, W. G.; Snyder, G. J.; Tremel, W. Effect of Isovalent
34
35 Substitution on the Thermoelectric Properties of the $\text{Cu}_2\text{ZnGeSe}_{4-x}\text{S}_x$. *J. Am. Chem. Soc.*
36
37 **2014**, *136*, 442–448.
38
39
40
41 (13) Shen, Y.; Li, C.; Huang, R.; Tian, R.; Ye, Y.; Pan, L.; Koumoto, K.; Zhang, R.; Wang, Y.
42
43 Eco-Friendly P-Type Cu_2SnS_3 Thermoelectric Material: Crystal Structure and Transport
44
45 Properties. *Sci. Rep.* **2016**, *6*, 32501.
46
47
48
49 (14) Suekuni, K.; Tsuruta, K.; Ariga, T.; Koyano, M. Thermoelectric Properties of Mineral
50
51 Tetrahedrites $\text{Cu}_{10}\text{Tr}_2\text{Sb}_4\text{S}_{13}$ with Low Thermal Conductivity. *Appl. Phys. Express* **2012**,
52
53 *5*, 51201.
54
55
56
57
58
59
60

- 1
2
3
4 (15) Lu, X.; Morelli, D. T.; Xia, Y.; Zhou, F.; Ozolins, V.; Chi, H.; Zhou, X.; Uher, C. High
5 Performance Thermoelectricity in Earth-Abundant Compounds Based on Natural Mineral
6 Tetrahedrites. *Adv. Energy Mater.* **2013**, *3*, 342–348.
7
8
9
10
11 (16) Barbier, T.; Lemoine, P.; Gascoin, S.; Lebedev, O. I.; Kaltzoglou, A.; Vaqueiro, P.;
12 Powell, A. V.; Smith, R. I.; Guilmeau, E. Structural Stability of the Synthetic
13 Thermoelectric Ternary and Nickel-Substituted Tetrahedrite Phases. *J. Alloys Compd.*
14 **2015**, *634*, 253–262.
15
16
17
18
19
20
21 (17) Suekuni, K.; Kim, F. S.; Nishiate, H.; Ohta, M.; Tanaka, H. I.; Takabatake, T. High-
22 Performance Thermoelectric Minerals: Colusites $\text{Cu}_{26}\text{V}_2\text{M}_6\text{S}_{32}$ (M = Ge, Sn). *Appl. Phys.*
23 *Lett.* **2014**, *105*, 132107.
24
25
26
27
28
29
30 (18) Bourgès, C.; Gilmas, M.; Lemoine, P.; Mordvinova, N.; Lebedev, O. I.; Hug, E.; Nassif,
31 V. M.; Malaman, B.; Daou, R.; Guilmeau, E. Structural Analysis and Thermoelectric
32 Properties of Mechanically Alloyed Colusites. *J. Mater. Chem. C* **2016**, *4*, 7455–7463.
33
34
35
36
37
38 (19) Kikuchi, Y.; Bouyrie, Y.; Ohta, M.; Suekuni, K.; Aihara, M.; Takabatake, T. Vanadium-
39 Free Colusites $\text{Cu}_{26}\text{A}_2\text{Sn}_6\text{S}_{32}$ (A = Nb, Ta) for Environmentally-Friendly Thermoelectrics.
40 *J. Mater. Chem. A* **2016**, *4*, 15207–15214.
41
42
43
44
45
46 (20) Qiu, P.; Zhang, T.; Qiu, Y.; Shi, X.; Chen, L. Sulfide Bornite Thermoelectric Material: A
47 Natural Mineral with Ultralow Thermal Conductivity. *Energy Environ. Sci.* **2014**, *7*, 4000.
48
49
50
51
52 (21) Guélou, G.; Powell, A. V.; Vaqueiro, P. Ball Milling as an Effective Route for the
53 Preparation of Doped Bornite: Synthesis, Stability and Thermoelectric Properties. *J.*
54 *Mater. Chem. C* **2015**, *3*, 10624–10629.
55
56
57
58
59
60

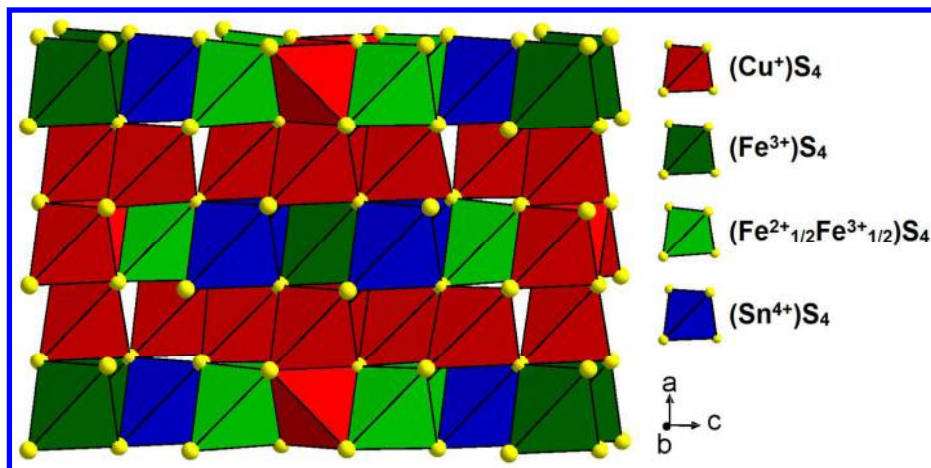
- 1
2
3
4
5
6
7
8
9
10
11
12
13
14
15
16
17
18
19
20
21
22
23
24
25
26
27
28
29
30
31
32
33
34
35
36
37
38
39
40
41
42
43
44
45
46
47
48
49
50
51
52
53
54
55
56
57
58
59
60
- (22) Kumar, V. P.; Barbier, T.; Lemoine, P.; Raveau, B.; Nassif, V.; Guilmeau, E. The Crucial Role of Selenium for Sulphur Substitution in the Structural Transitions and Thermoelectric Properties of Cu_5FeS_4 Bornite. *Dalt. Trans.* **2017**, *46*, 2174.
- (23) Kudoh, Y.; Takeuchi, Y. The Superstructure of Stannoidite. *Zeitschrift fur Krist.* **1976**, *144*, 145–160.
- (24) Lee, M. S.; Takenouchi, S.; Imai, H. Syntheses of Stannoidite and Mawsonite and Their Genesis in Ore Deposits. *Econ. Geol.* **1975**, *70*, 834–843.
- (25) Yamanaka, T.; Kato, A. Mossbauer Effect Study of ^{57}Fe and ^{119}Sn in Stannite, Stannoidite, and Mawsonite. *Am. Mineral.* **1976**, *61*, 260–265.
- (26) Suryanarayana, C. Mechanical Alloying and Milling. *Prog. Mater. Sci.* **2001**, *46*, 1–184.
- (27) Rodríguez-Carvajal, J. Recent Advances in Magnetic Structure Determination by Neutron Powder Diffraction. *Phys. B Condens. Matter* **1993**, *192*, 55–69.
- (28) Roisnel, T.; Rodríguez-Carvajal, J. WinPLOTR: A Windows Tool for Powder Diffraction Pattern Analysis. *Mater. Sci. Forum* **2001**, *378–381*, 118–123.
- (29) Alleno, E.; Bérardan, D.; Byl, C.; Candolfi, C.; Daou, R.; Decourt, R.; Guilmeau, E.; Hébert, S.; Hejtmanek, J.; Lenoir, B.; et al. Invited Article: A Round Robin Test of the Uncertainty on the Measurement of the Thermoelectric Dimensionless Figure of Merit of $\text{Co}_{0.97}\text{Ni}_{0.03}\text{Sb}_3$. *Rev. Sci. Instrum.* **2015**, *86*, 11301.
- (30) Barbier, T.; Rollin-Martinet, S.; Lemoine, P.; Gascoin, F.; Kaltzoglou, A.; Vaqueiro, P.; Powell, A. V.; Guilmeau, E. Thermoelectric Materials: A New Rapid Synthesis Process

- 1
2
3 for Nontoxic and High-Performance Tetrahedrite Compounds. *J. Am. Ceram. Soc.* **2016**,
4
5 99, 51–56.
6
7
8
9 (31) Barbier, T.; Lemoine, P.; Martinet, S.; Eriksson, M.; Gilmas, M.; Hug, E.; Guelou, G.;
10
11 Vaqueiro, P.; Powell, A. V.; Guilmeau, E. Up-Scaled Synthesis Process of Sulphur-Based
12
13 Thermoelectric Materials. *RSC Adv.* **2016**, 6, 10044–10053.
14
15
16
17 (32) Bourgès, C.; Lemoine, P.; Lebedev, O. I.; Daou, R.; Hardy, V.; Malaman, B.; Guilmeau,
18
19 E. Low Thermal Conductivity in Ternary $\text{Cu}_4\text{Sn}_7\text{S}_{16}$ Compound. *Acta Mater.* **2015**, 97,
20
21 180–190.
22
23
24
25 (33) Eibschütz, M.; Hermon, E.; Shtrikman, S. Determination of Cation Valencies in
26
27 $\text{Cu}_2\text{FeSnS}_4$ by Mossbauer Effect and Magnetic Susceptibility Measurements. *J. Phys.*
28
29 *Chem. Solids* **1967**, 28, 1633–1638.
30
31
32
33 (34) Lippens, P. E. Interpretation of the ^{119}Sn Mössbauer Isomer Shifts in Complex Tin
34
35 Chalcogenides Sn Mo. *Phys. Rev. B* **1999**, 60, 4576–4586.
36
37
38
39 (35) Murad, E. Mössbauer Spectroscopy of Clays, Soils and Their Mineral Constituents. *Clay*
40
41 *Miner.* **2010**, 45, 413–430.
42
43
44
45 (36) Pavan Kumar, V.; Guilmeau, E.; Raveau, B.; Caignaert, V.; Varadaraju, U. V. A New
46
47 Wide Band Gap Thermoelectric Quaternary Selenide $\text{Cu}_2\text{MgSnSe}_4$. *J. Appl. Phys.* **2015**,
48
49 118, 155101.
50
51
52
53 (37) Liu, M.-L.; Chen, I.-W.; Huang, F.-Q.; Chen, L.-D. Improved Thermoelectric Properties
54
55 of Cu-Doped Quaternary Chalcogenides of $\text{Cu}_2\text{CdSnSe}_4$. *Adv. Mater.* **2009**, 21, 3808–
56
57
58
59
60

1
2
3 3812.
4
5

- 6
7 (38) Suekuni, K.; Kim, F. S.; Takabatake, T. Tunable Electronic Properties and Low Thermal
8
9 Conductivity in Synthetic Colusites $\text{Cu}_{26-x}\text{Zn}_x\text{V}_2\text{M}_6\text{S}_{32}$ ($x \leq 4$, M= Ge, Sn). *J. Appl. Phys.*
10
11 **2014**, *116*, 63706.
12
13
14
15 (39) Zhang, R.; Chen, K.; Du, B.; Reece, M. J. Screening for Cu–S Based Thermoelectric
16
17 Materials Using Crystal Structure Features. *J. Mater. Chem. A* **2017**, *5*, 5013.
18
19
20
21
22
23
24
25
26
27
28
29
30
31
32
33
34
35
36
37
38
39
40
41
42
43
44
45
46
47
48
49
50
51
52
53
54
55
56
57
58
59
60

TOC Graphic



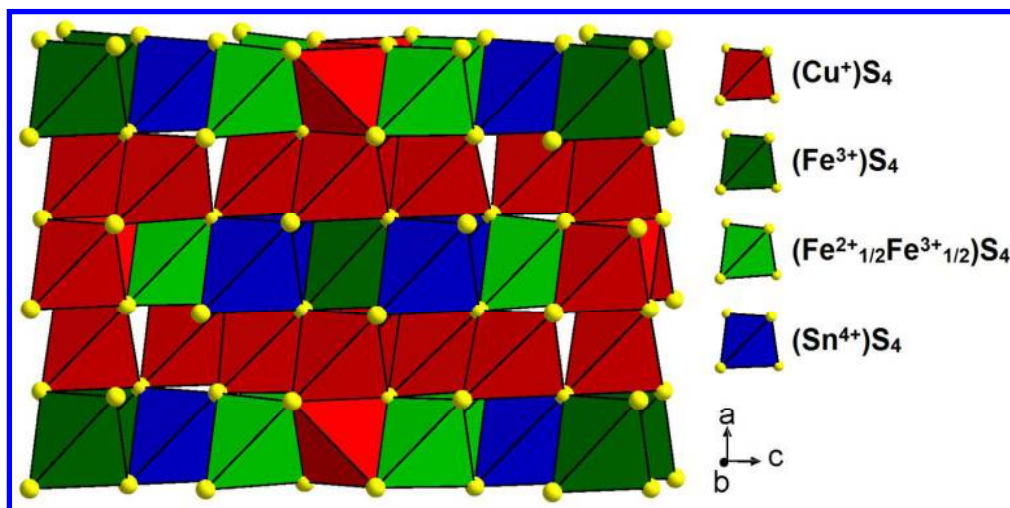


Figure 1. View of the crystal structure of stannoidite Cu₈Fe₃Sn₂S₁₂.

439x216mm (95 x 95 DPI)

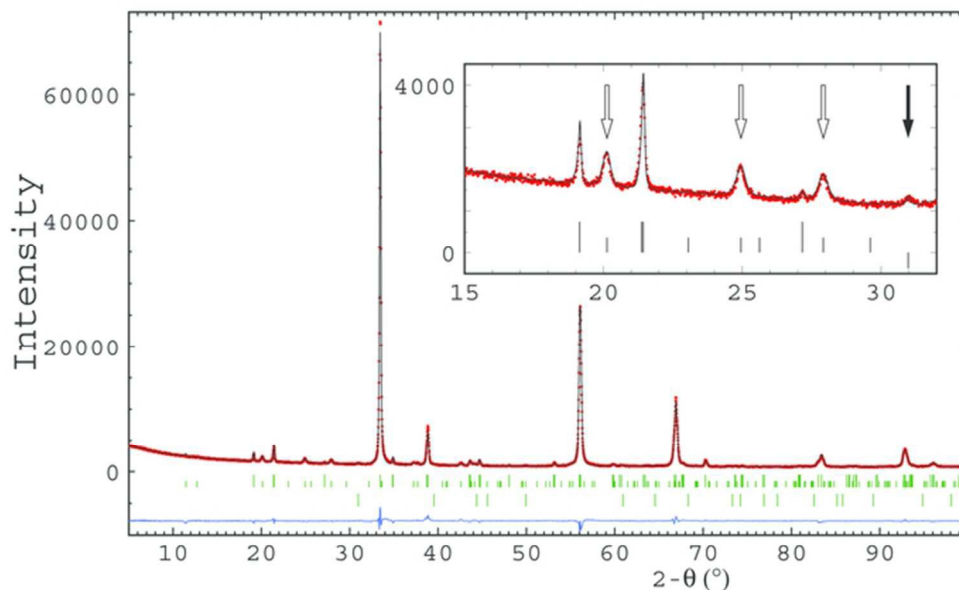


Figure 2. Rietveld refinement of $\text{Cu}_8\text{Fe}_3\text{Sn}_2\text{S}_{12}$: as usual, red dots, black and blue curves represent the observed, calculated and difference plots, respectively. The green vertical lines represent the position of the Bragg reflections. Top lines are reflections of the stannoidite: short lines are $h,k,l=3n+1$ and $h,k,l=3n+2$ reflections while large lines are $h,k,l=3n$ reflections. Bottom lines are reflections of the SnO_2 impurity. The inset shows the broadening of the h,k,l reflections with $l=3n+1$ and $l=3n+2$ (white arrows) and the main reflection of the SnO_2 impurity (black arrow).

60x47mm (300 x 300 DPI)

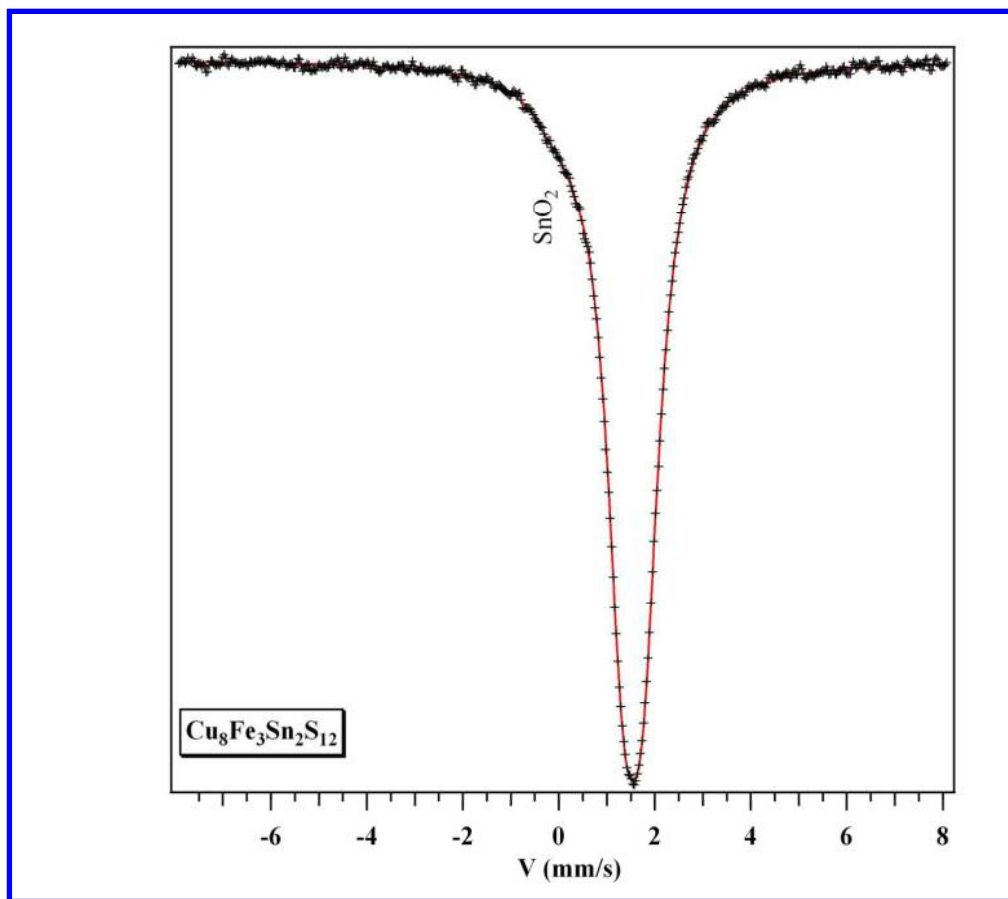


Figure 3. RT ^{119}Sn Mössbauer spectrum of $\text{Cu}_8\text{Fe}_3\text{Sn}_2\text{S}_{12}$

142x125mm (300 x 300 DPI)

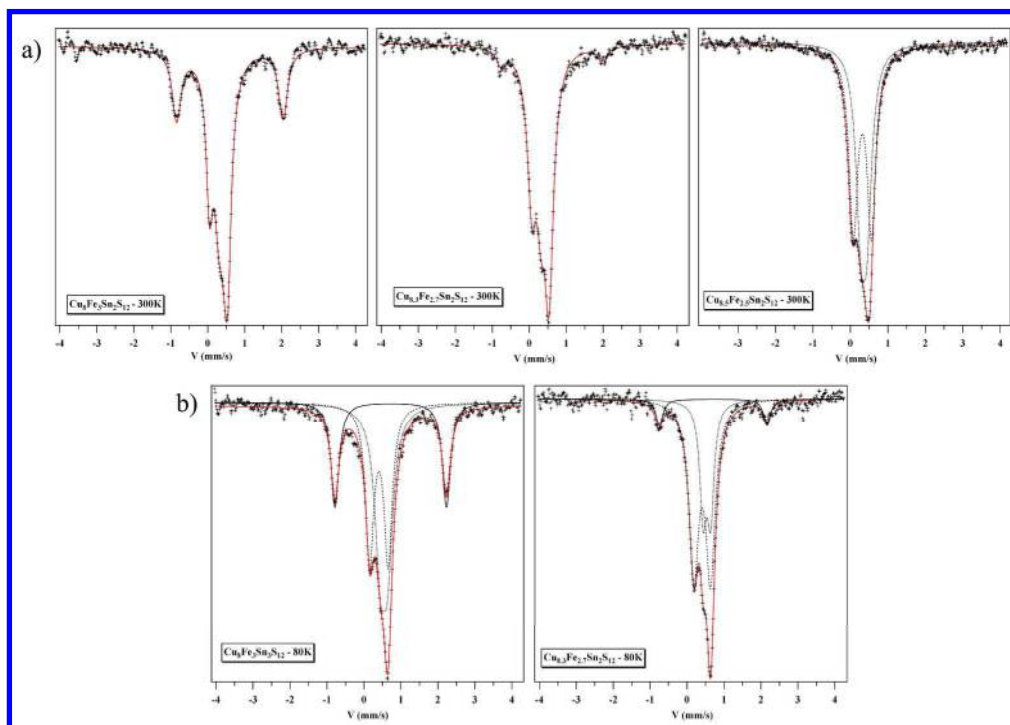


Figure 4. ^{57}Fe Mössbauer spectra of $\text{Cu}_{8+x}\text{Fe}_{3-x}\text{Sn}_2\text{S}_{12}$ with x increasing from left to right (a) top row, at 300 K for $x = 0, 0.3$ and 0.5 and b) bottom row, at 100 K for $x = 0$ and 0.3

288x204mm (300 x 300 DPI)

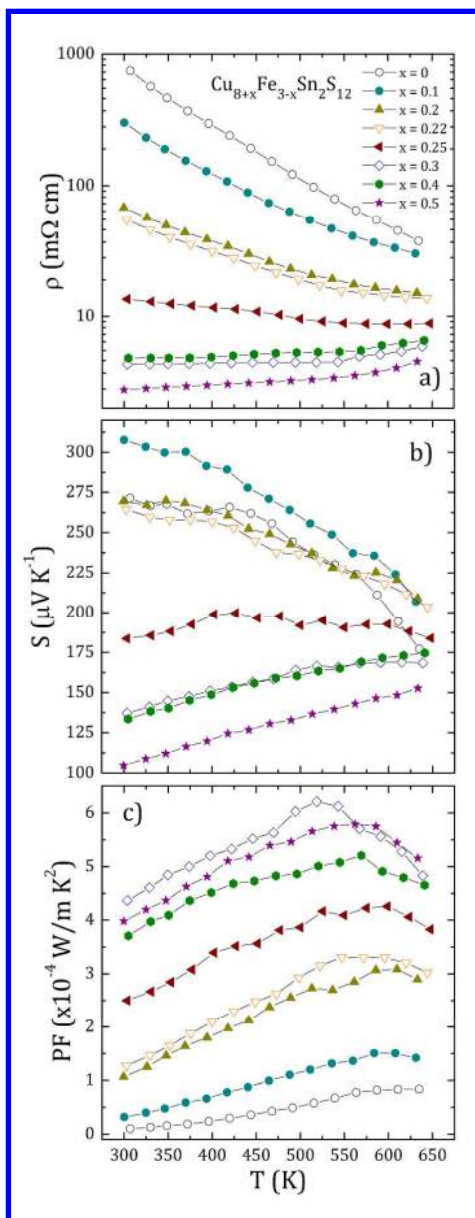


Figure 5. Temperature dependence of (a) electrical resistivity, (b) Seebeck coefficient and (c) power factor in the $\text{Cu}_{8+x}\text{Fe}_{3-x}\text{Sn}_2\text{S}_{12}$ series.

199x517mm (299 x 299 DPI)

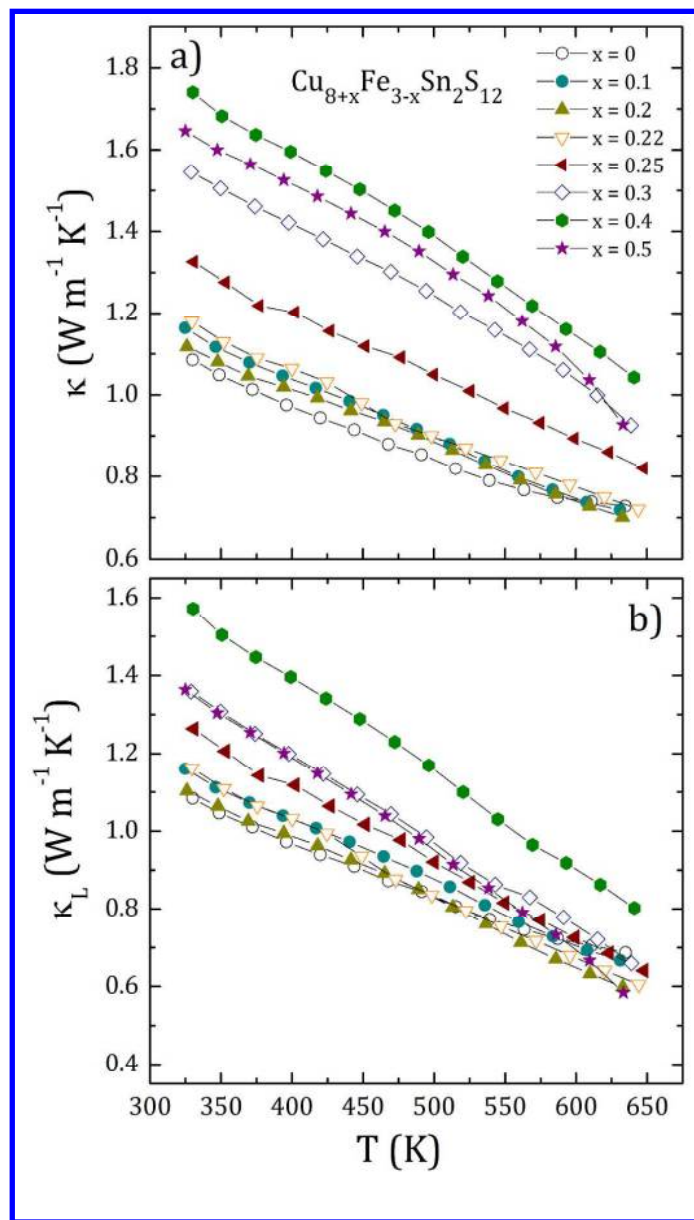


Figure 6. Temperature dependence of (a) thermal conductivity and (b) lattice thermal conductivity in the $\text{Cu}_{8+x}\text{Fe}_{3-x}\text{Sn}_2\text{S}_{12}$ series.

196x344mm (299 x 299 DPI)

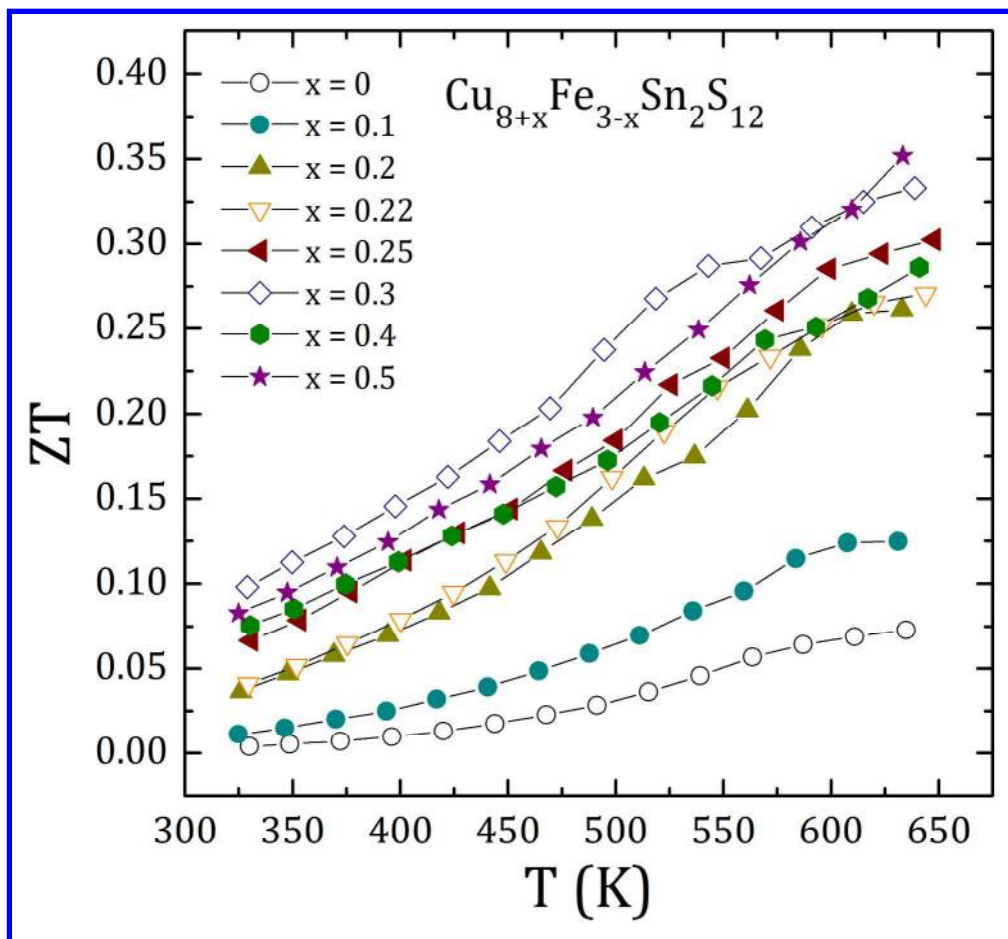


Figure 7. Temperature dependence of the figure of merit ZT in the $\text{Cu}_{8+x}\text{Fe}_{3-x}\text{Sn}_2\text{S}_{12}$ series.

189x175mm (299 x 299 DPI)